Effect of the galactic halo modeling on the DAMA-NaI annual modulation result:
An extended analysis of the data for weakly interacting massive particles
with a purely spin-independent coupling

P. Belli,[1,*] R. Cerulli,[1,†] N. Fornengo,[2,‡] and S. Scopel[2,§]

[1] *Dipartimento di Fisica, Università di Roma "Tor Vergata" and INFN, Sezione di Roma2, I-00133 Roma, Italy*
[2]*Dipartimento di Fisica Teorica, Università di Torino and INFN, Sezione di Torino, Via P. Giuria 1, I-10125 Torino, Italy*

The DAMA-NaI Collaboration has observed a 4σ C.L. model-independent effect investigating the annual modulation signature in the counting rate of an NaI(Tl) setup (total exposure of 57986 kg day) and the implications of this effect have been studied under different model-dependent assumptions. In this paper we extend one of the previous analyses, the case of a WIMP with a purely spin-independent coupling, by discussing in detail the implications on the results of the uncertainties on the dark matter galactic velocity distribution. We study in a systematic way possible departures from the isothermal sphere model, which is the parametrization usually adopted to describe the halo. We specifically consider modifications arising from various matter density profiles, effects due to anisotropies of the velocity dispersion tensor and rotation of the galactic halo. The hypothesis of WIMP annual modulation, already favored in the previous analysis using an isothermal sphere, is confirmed in all the investigated scenarios, and the effects of the different halo models on the determination of the allowed maximum-likelihood region in the WIMP mass and WIMP-nucleon cross section are derived and discussed.

I. INTRODUCTION

In the last few years various technical approaches have been exploited in direct searches for weakly interacting massive particles (WIMP) [1]. In particular, the DAMA-NaI Collaboration has collected a very large body of statistics which allows one to look for the distinctive signature in dark matter (DM) direct detection represented by the annual modulation of the rate [2–4], an effect which is due to the rotation of the Earth around the Sun [5]. The analysis of the DAMA-NaI data after 4 years of running [2,4], corresponding to a total exposure of 57986 kg day, has indeed led to the observation of an annual-modulation effect, which does not appear to be related to any possible source of systematics [3]. This exciting result has been analyzed under different hypotheses on the properties of WIMP dark matter: purely spin independent coupling [2], mixed spin-coherent interaction [6], inelastic dark matter [7]. In the case of purely spin-independent interactions, the annual modulation result has been shown to be compatible with a galactic halo composed, at least partially, by relic neutralinos in different classes of supersymmetric models [8,9].

In the present analysis we consider the case of a WIMP with coherent interactions dominant over the spin-dependent ones. The analysis of the counting rate of any direct detection experiment may be done in terms of the WIMP mass m_W and of the quantity $\xi\sigma_{\text{scalar}}^{(\text{nucleon})}$, where $\sigma_{\text{scalar}}^{(\text{nucleon})}$ is the WIMP-nucleon cross section for scalar interaction and ξ^1 is the fractional amount of local nonbaryonic DM density which is ascribed to the WIMP responsible for the effect ($\xi\leq1$) [2,8]. Performing a maximum-likelihood analysis of the data, the DAMA-NaI Collaboration has derived a region in the plane m_W-$\xi\sigma_{\text{scalar}}^{(\text{nucleon})}$ which is compatible at 3σ C.L. to the observed effect of annual modulation. The properties of this region are sensitive to astrophysical inputs [4,10], some of which deserve a reanalysis and a deeper insight.

One of the main ingredients for the calculation of the expected rates is the distribution function of WIMPs in their six-dimensional phase space: $F(\vec{r},\vec{v})d^3r\,d^3v$ [where the position vector $\vec{r}\equiv(x,y,z)$ and the velocity vector $\vec{v}\equiv(v_x,v_y,v_z)$ are defined in the rest frame of the Galaxy]. Direct detection rates R_{det} depend on the distribution function (DF) at the Earth position in the Galaxy:

$$f(\vec{v})\equiv F(\vec{R}_0,\vec{v}),\qquad(1)$$

where $\vec{R}_0\equiv(R_0,0,0)$ is the location of the Earth at a distance $R_0\simeq8.5$ kpc from the galactic center and along the galactic plane. It is therefore clear that an accurate calculation of the expected detection rates requires a knowledge of the phase-space distribution function $F(\vec{r},\vec{v})d^3r\,d^3v$.

From the observational side, the most relevant piece of information coming from astrophysics is related to the rotational velocity of objects bounded to the Galaxy:

$$v_{rot}^2(r)=\frac{GM_{tot}(r)}{r},\qquad(2)$$

---

*Electronic address: belli@roma2.infn.it

†Electronic address: cerulli@roma2.infn.it

‡Electronic address: fornengo@to.infn.it;
URL: http://www.to.infn.it/~fornengo/

§Electronic address: scopel@to.infn.it

---

[1]In Ref. [2] the same symbol indicates a different quantity: $\xi=\rho_W/(0.3\ \text{GeV cm}^{-3})$.

where G is Newton's constant and $M_{tot}(r)$ denotes the total mass contained inside the radius $r \equiv |\vec{r}|$:

$$M_{tot}(r) = \int_{r' < r} d^3 r' \, \rho_{tot}(\vec{r}'). \qquad (3)$$

The rotational velocity therefore depends on the total matter density distribution in space:

$$\rho_{tot}(\vec{r}) = \rho_{DM}(\vec{r}) + \rho_{vis}(\vec{r}), \qquad (4)$$

where the DM density distribution function is

$$\rho_{DM}(\vec{r}) \equiv \int d^3 v \, F(\vec{r}, \vec{v}), \qquad (5)$$

and $\rho_{vis}(\vec{r})$ represents the contribution to the matter density due to components other than the DM, like the disk and the bulge. The local values for the rotational velocity and for the DM matter density are denoted by $v_0 \equiv v_{rot}(\vec{R}_0)$ and $\rho_0 \equiv \rho_{DM}(\vec{R}_0)$ and they represent two key parameters in the calculation of WIMP direct detection rates, as it will be discussed in the following.

In order to calculate the DF of Eq. (1) one must invert Eq. (5) taking into account observational data. This problem is affected by degeneracies that cannot be solved without adding some piece of information. This explains why the velocity distribution represents one of the main sources of uncertainty in the calculation of direct detection signals.

The usual approach to this problem consists in assuming that the system has some symmetry and that the distribution F depends on the phase space parameters only through some integrals of motion (energy, angular momentum): this last condition automatically implies stationarity and that the Jeans' equations are verified [11]. The velocity ellipsoid $\sigma_{ij} \equiv \langle v_i v_j \rangle$ may then be calculated as a function of the derivatives of the potential (which are related to the rotational velocity) by making use of Euler's equation [11]. Physically, this corresponds to imposing hydrostatic equilibrium between pressure and gravitational attraction.

The most common and widely used example of such a procedure, and by far the simplest, is the isothermal sphere model. It consists in a spherical infinite system with a flat rotational curve, which automatically implies $\rho(r) \propto r^{-2}$ and the potential $\Psi \propto \ln(r^2)$. The DF may be easily worked out, and turns out to be a Maxwellian: $f(v) \propto \exp(-3v^2/(2v_{rms}^2))$, where $v \equiv |\vec{v}|$ and v_{rms} denotes the root mean squared velocity of the WIMPs. The isothermal sphere describes a self-gravitating gas of collisionless particles in thermal equilibrium, representing the highest entropy rearrangement of WIMPs in their phase space. A strong argument in favor of this last property is the "violent relaxation" model of Lynden-Bell [12], which indicates that the violently changing gravitational field of the newly formed Galaxy may have led the non-interacting WIMPs to thermal equilibrium. Hydrostatic equilibrium and the assumption that the velocity ellipsoid is isotropic allows to calculate v_{rms} through the relation: $v_{rms}^2 = 3/2 v_{rot}^2(R_0)$. Due to its simplicity, the isothermal sphere model has become the "standard" assump-

tion in the evaluation of DM expected rates, and has been used extensively in the literature, including the analysis of the DAMA-NaI modulation data [2]. However many of its underlying assumptions (sphericity of the halo, absence of rotation, isotropy of the dispersion tensor, flatness of the rotational curve) are not strongly constrained by astrophysical observations. Moreover the isothermal sphere is strictly unphysical and can only represent the behavior of the inner part of physical systems, since it has a total infinite mass and needs some cutoff at large radii.

In light of the latest experimental data on WIMP direct searches, the issue of possible departures from the isothermal sphere model has gained interest and prompted several discussions [4,10,13]. In the present paper we intend to analyze this issue in a systematic way, by employing a comprehensive set of self-consistent galactic halo models. Each model introduces a different degree of deviation from the simple isothermal sphere. We consider modifications in the velocity distribution function which are originated from a change of the gravitational potential or a change of the DM density profile [14–20]. We classify the different models depending on the symmetry properties of the galactic halo: spherical potential/density profile with an isotropic velocity dispersion; spherical potential/density profile with a nonisotropic velocity dispersion; axisymmetric models; triaxial models. For the axisymmetric models we also consider the possibility of having a co-rotating or counter-rotating halo.

The plan of the paper is as follows. In Sec. II we introduce the formalism for the calculation of direct detection rates and the annual modulation signal, and summarize the procedure used by the DAMA-NaI Collaboration to determine the annual modulation region in the plane m_W-$\xi \sigma_{scalar}^{(nucleon)}$ for a purely spin-independent interacting WIMP. In Sec. III we describe the halo models that we intend to discuss and introduce a naming scheme that will be used throughout the paper. Section IV is devoted to the discussion of the constraints on the dark halo of our Galaxy coming from available observational data. In Sec. V the annual modulation region is calculated in a systematic way for all the models previously introduced, and the results are discussed. Finally, Sec. VI is devoted to our conclusions.

II. DIRECT DETECTION RATES AND ANNUAL MODULATION EFFECT

The expected differential event rate of a WIMP direct search experiment is given, for a monatomic detector, by the expression

$$\frac{dR_{det}}{dE_R} = N_T \frac{\rho_0}{m_W} \int d\vec{w} f(\vec{w}) w \frac{d\sigma}{dE_R}(w, E_R) \qquad (6)$$

where N_T is the number of the target nuclei per unit of mass, m_W is the WIMP mass, $\vec{w}$ and $f(\vec{w})$ denote the WIMP velocity and DF in the Earth frame ($w = |\vec{w}|$), $d\sigma/dE_R$ is the WIMP-nucleus differential cross section and E_R is the nuclear recoil energy. Notice that the detection rate is di-

rectly proportional to the local DM density ρ_0. The generalization of Eq. (6) to a diatomic detector, like NaI, is straightforward.

The differential cross section is, in general, a sum of a coherent and a spin-dependent contribution. In this paper we consider only the case of a WIMP whose interactions are dominated by the coherent part. In this case the rate may be expressed in terms of the WIMP-nucleon scalar cross section, $\sigma_{scalar}^{(nucleon)}$, as

$$\frac{d\sigma}{dE_R} \simeq \left(\frac{d\sigma}{dE_R}\right)_{coherent}$$

$$\simeq \frac{F_n^2(E_R)}{E_R^{max}} \left(\frac{1+m_W/m_p}{1+m_W/m_N}\right)^2 A^2 \sigma_{scalar}^{(nucleon)}, \qquad (7)$$

where m_p and m_N are the proton and nucleus mass, A is the nuclear mass number, E_R^{max} is the maximal recoil energy and $F_n(E_R)$ is the nuclear form factor for coherent interactions which may be parametrized with the usual Helm expression [21].

The relation between the velocities $\vec{v}$ and $\vec{w}$ is given by

$$\vec{v} = \vec{v}_\oplus + \vec{w}, \qquad (8)$$

$$\vec{v}_\oplus = \vec{v}_\odot + \vec{v}_{\oplus rot}, \qquad (9)$$

where $\vec{v}_\oplus$ and $\vec{v}_\odot$ denote the velocities of the Earth and the Sun in the Galactic rest frame ($|\vec{v}_\odot| \simeq v_0 + 12$ km/sec), and $\vec{v}_{\oplus rot}$ is the Earth's orbital velocity around the Sun ($|\vec{v}_{\oplus rot}| = 30$ km/sec). Projecting Eq. (9) in the galactic plane, one gets

$$|\vec{v}_\oplus| = |\vec{v}_\odot| + |\vec{v}_{\oplus rot}|\cos\gamma\cos[\omega(t-t_0)] \qquad (10)$$

where γ is the inclination of the plane of rotation with respect to the galactic one, $\omega = 2\pi/T$ with $T = 1$ year, and $t_0 \simeq 2^{nd}$ June corresponds to the day when the Earth's velocity is at its maximum.

The change of reference frame of Eqs. (8), (9), (10) introduces through the DF $f(\vec{w})$ a time dependence in the expected rate R_{det}. In order to exploit this time-dependence to extract the modulated signal from the measured counting rates, we follow the maximal-likelihood procedure of Ref. [2], to which we refer for a detailed discussion. This procedure allows to determine the region in the plane (m_W-$\xi\sigma_{scalar}^{(nucleon)}$) which is compatible with the modulation signal. A lower bound on m_W at the value $m_W = 30$ GeV is applied, to conform to the analysis of Refs. [2,4].

The data we analyze in the present paper refer to the full set of data released so far by the DAMA-NaI Collaboration [2] (DAMA-NaI 0–4), including also the upper limit on $\xi\sigma_{scalar}^{(nucleon)}$ obtained by the same Collaboration, as discussed in Ref. [2]. The same values of the quenching factors and of the cut efficiences as in Refs. [2,4] are used. We stress that also the determination of upper limits is affected by the choice of the WIMPs DF. This means that also when con-

fronting upper limits one has to specify the galactic halo models which have been considered in the calculation. The formalism introduced in the present paper may in fact be used also to quantify the uncertainty in the determination of upper limits from direct detection experiments.

III. HALO MODELS

Let us turn now to the discussion of the galactic halo models and of the techniques used to calculate the velocity distribution function $f(\vec{v})$. The different models are classified according to the symmetry properties of their matter density profile (or gravitational potential) and of the velocity distribution function. We define four classes: (A) spherically symmetric matter density with isotropic velocity dispersion; (B) spherically symmetric matter density with nonisotropic velocity dispersion; (C) axisymmetric models; (D) triaxial models. All the models which we describe in this section, and that will be used in the rest of the paper, are summarized in Table II, where we also introduce a naming scheme that will be of practical use in the discussion.

A. Spherically symmetric matter density with isotropic velocity dispersion

The first class of models is represented by those with a spherically symmetric matter density $\rho(\vec{r}) = \rho(r)$ and isotropic velocity distribution $f(\vec{v}) = f(v)$. These two conditions imply that the phase-space DF depends on the space and velocity variables only through the energy, which is an integral of motion: $F(\vec{r}, \vec{v}) = F(\epsilon)$, where $\epsilon = \Psi(r) - v^2/2$ is the relative energy (per unit mass) of the WIMP and Ψ is the relative potential, related to the total density ρ_{tot} through Poisson's equation [11]:

$$\nabla^2\Psi = -4\pi G\rho_{tot}. \qquad (11)$$

Notice that ρ_{tot} refers to all the matter components of the Galaxy, like the disk, the bulge or the halo, as written in Eq. (4).

Once the total potential $\Psi(r)$ is known, the WIMP DF $F(\epsilon)$ may be worked out by inverting Eq. (5). A change of variables from r to Ψ allows to cast Eq. (5) as [11]

$$4\pi\int_0^\Psi F(\epsilon)\sqrt{2(\Psi-\epsilon)}d\epsilon = \rho_{DM}(\Psi). \qquad (12)$$

By performing a Laplace inversion on Eq. (12), one obtains the Eddington formula [11]:

$$F(\epsilon) = \frac{1}{\sqrt{8}\pi^2}\frac{d}{d\epsilon}\int_0^\epsilon \frac{d\rho_{DM}(\Psi)}{d\Psi}\frac{d\Psi}{\sqrt{\epsilon-\Psi}}. \qquad (13)$$

In Eqs. (12), (13) the normalization of Ψ, which is defined through Poisson's equation up to an arbitrary constant, is fixed by requiring that $\Psi(\infty) = 0$. The velocity distribution function $f(v)$ which enters the calculation of direct detection rates is then obtained as in Eq. (1).

TABLE I. Values of the parameters for the spherically symmetric density profile of Eq. (26).

	α	β	γ	a (kpc)
NFW [18]	1	3	1	20
Moore *et al.* [19]	1.5	3	1.5	28
Kravtsov *et al.* [20]	2	3	0.4	10
Jaffe [14]	1	4	2	160

Equation (13) shows that the dark matter DF $F(\vec{r},\vec{v})$ depends not only on the halo DM density distribution ρ_{DM}, but also on the density distribution of all the other galactic components. This has to be the case, since the DM particles move inside the gravitational potential generated by all the matter that makes up the Galaxy. A complete and rigorous determination of the DM DF will therefore require to model not only the galactic halo, but also all the other (disk, bulge) components of the Galaxy (see, for instance Ref. [22]).

However, WIMP direct detection is directly sensitive only to local properties of the Galaxy, and in particular the relevant parameters in the calculation of the detection rate are the local rotational velocity v_0 and the local DM matter density ρ_0. In fact, v_0 is directly related to the average WIMP kinetic energy, which is relevant in the scattering process with the nuclei of the detector, and the change of reference frame of Eqs. (8), (9), which is crucial in determining the amount of annual modulation in the detection rate. Instead, ρ_0 is a sort of normalization factor for the direct detection rate R_{det}. The dependence of R_{det} essentially on local parameters implies that a detailed modeling of the inner ($r \ll R_0$) part of the Galaxy, where the disk and bulge components are more relevant and in general dominant over the halo, is not crucial for our analysis. Moreover, the matter density of nonhalo components at the local position in the Galaxy ($r=R_0$) is no longer dominant with respect to the halo matter density at the same position (see, for instance Ref. [22]). The bulge, in fact, can be described by using a spheroidal density distribution which gives a sizeable contribution inside the first kpc from the galactic center, and it is truncated at about $r \simeq 2$ kpc. The disk has an exponential distribution which in most of the models dies away at about 4 kpc from the galactic center. We will therefore assume in the following that in the outer Galaxy the dominant contribution to the matter density is given by the halo

$$\rho_{vis} \ll \rho_{DM} \quad \text{for} \quad r \gtrsim R_0. \tag{14}$$

The only basic information which is required from the nonhalo components is their contribution to the local rotational velocity v_0:

$$v_0^2 = v_{rot}^2(R_0) = \frac{G}{R_0}[M_{vis} + M_{halo}], \tag{15}$$

where

$$M_{vis(halo)} \equiv \int_{r'<R_0} d^3 r' \rho_{vis(halo)}(r'). \tag{16}$$

A maximal halo occurs when $M_{vis} \ll M_{halo}$: in this case almost all the local rotational velocity is supported by the halo and the local DM density ρ_0 gets its maximal value ρ_0^{max} compatible with the given v_0. The opposite situation occurs when M_{vis} assumes its maximal value compatible with observations: in this case, the local rotational velocity gets the maximal contribution from the nonhalo components and only a fraction of v_0 is supported by the halo. At the same time ρ_0 gets its minimal value ρ_0^{min}, for the same v_0. The constraints on these parameters are discussed in Sec. IV.

From the point of view of calculating the DM DF [Eq. (13)], the occurrence of a maximal or nonmaximal halo modifies the gravitational potential $\Psi(r)$ and therefore the velocity distribution function $f(v)$ is affected. Indicating with $\Psi_0(r)$ the potential for the maximal halo, the condition of Eq. (14) allows the generalization to the nonmaximal case as:

$$\Psi(r) = \frac{\rho_0}{\rho_0^{max}} \Psi_0(r) + \left(1 - \frac{\rho_0}{\rho_0^{max}} \right) \frac{R_0}{r} v_0^2. \tag{17}$$

The condition of Eq. (14) allows to work out the total potential for the case of nonmaximal halos without explicitly modeling the visible parts of the Galaxy (bulk, disk): all the dependence of these components is contained in M_{vis}.

As a comment, we notice that the presence of a nonnegligible contribution to v_0 from the nonhalo components alters also the velocity distribution function of the isothermal sphere. The standard Maxwellian form for the isothermal sphere is in fact correct only for a maximal halo.

Now that we have discussed the procedure to calculate the velocity distribution function once the matter density of the DM is given, we proceed to introduce the different models.

The first type of model is a direct generalization of the isothermal sphere by introducing a core radius R_c (model A1). The density profile is

$$\rho_{DM}(r) = \frac{v_0^2}{4\pi G} \frac{3R_c^2 + r^2}{(R_c^2 + r^2)^2}, \tag{18}$$

which corresponds to the following potential for a maximal halo:

$$\Psi_0(r) = -\frac{v_0^2}{2} \ln(R_c^2 + r^2). \tag{19}$$

From the analytic form of this potential we will refer to this type of model as a *logarithmic model*. The usual isothermal sphere (model A0) corresponds to the limit $R_c \to 0$:

$$\rho_{DM}(r) = \frac{v_0^2}{4\pi G} \frac{1}{r^2}, \tag{20}$$

which corresponds to the following potential for a maximal halo:

$$\Psi_0(r) = -\frac{v_0^2}{2} \ln(r^2). \tag{21}$$

TABLE II. Summary of the galactic halo models discussed in Sec. III. The label introduced in the first column is used throughout the text to indicate each model in a unique way. For all the models, the numerical values of the parameters which have been used in the calculations are given in the third column. The last column contains references to the models in the text. Models of class C have been analyzed also including co-rotation and counter-rotation of the halo through Eq. (42).

Class A: Spherical ρ_{DM}, isotropic velocity dispersion

A0	Isothermal sphere		Eq. (20)
A1	Evans' logarithmic [15]	$R_c = 5$ kpc	Eq. (18)
A2	Evans' power-law [16]	$R_c = 16$ kpc, $\beta = 0.7$	Eq. (23)
A3	Evans' power-law [16]	$R_c = 2$ kpc, $\beta = -0.1$	Eq. (23)
A4	Jaffe [14]	Table I	Eq. (26)
A5	NFW [18]	Table I	Eq. (26)
A6	Moore *et al.* [19]	Table I	Eq. (26)
A7	Kravtsov *et al.* [20]	Table I	Eq. (26)

Class B: Spherical ρ_{DM}, non-isotropic velocity dispersion (Osipkov-Merrit, $\beta_0 = 0.4$)

B1	Evans' logarithmic	$R_c = 5$ kpc	Eqs. (18),(28)
B2	Evans' power-law	$R_c = 16$ kpc, $\beta = 0.7$	Eqs. (23),(28)
B3	Evans' power-law	$R_c = 2$ kpc, $\beta = -0.1$	Eqs. (23),(28)
B4	Jaffe	Table I	Eqs. (26),(28)
B5	NFW	Table I	Eqs. (26),(28)
B6	Moore *et al.*	Table I	Eqs. (26),(28)
B7	Kravtsov *et al.*	Table I	Eqs. (26),(28)

Class C: Axisymmetric ρ_{DM}

C1	Evans' logarithmic	$R_c = 0$, $q = 1/\sqrt{2}$	Eqs. (33),(34)
C2	Evans' logarithmic	$R_c = 5$ kpc, $q = 1/\sqrt{2}$	Eqs. (33),(34)
C3	Evans' power-law	$R_c = 16$ kpc, $q = 0.95$, $\beta = 0.9$	Eqs. (37),(38)
C4	Evans' power-law	$R_c = 2$ kpc, $q = 1/\sqrt{2}$, $\beta = -0.1$	Eqs. (37),(38)

Class D: Triaxial ρ_{DM} [17] ($q = 0.8, p = 0.9$)

D1	Earth on major axis, radial anisotropy	$\delta = -1.78$	Eqs. (43),(44)
D2	Earth on major axis, tangential anis.	$\delta = 16$	Eqs. (43),(44)
D3	Earth on intermediate axis, radial anis.	$\delta = -1.78$	Eqs. (43),(44)
D4	Earth on intermediate axis, tangential anis.	$\delta = 16$	Eqs. (43),(44)

For a maximal halo, the velocity distribution function arising from Eqs. (20), (21) is the standard Maxwellian one. For a nonmaximal halo, a deviation is present also in the $R_c \to 0$, as discussed above. The rotational curve supported by Ψ_0 of Eq. (19) is:

$$v_{rot}^2(r) = v_0^2 \frac{r^2}{(R_c^2 + r^2)}. \qquad (22)$$

It is rising for small radii and at large radii becomes flat. In the $R_C \to 0$ limit, $v_{rot} = v_0$ for all radii.

A second type of spherical model (A2 and A3) is defined by the following matter density [16]:

$$\rho_{DM}(r) = \frac{\beta \Psi_a R_c^\beta}{4\pi G} \frac{3R_c^2 + r^2(1 - \beta)}{(R_c^2 + r^2)^{(\beta+4)/2}}, \qquad (23)$$

which corresponds to the following potential for a maximal halo:

$$\Psi_0(r) = \frac{\Psi_a R_c^\beta}{(R_c^2 + r^2)^{\beta/2}} \quad (\beta \neq 0). \qquad (24)$$

From the analytic form of this potential we will refer to this type of model as a *power-law model*. It represents the spherical limit of the more general class of axisymmetric "power-law" model of Ref. [16] which will be discussed in Sec. III B. The family of power-law models given by Eq. (24) is not defined for $\beta = 0$. However, when $\beta = 0$ is substituted in Eq. (23), the density of Eq. (18) is recovered. In fact the logarithmic model turns out to have the properties of the "missing" $\beta = 0$ power law potential. Evaluating Eq. (23) for $r = R_0$ the parameter Ψ_a can be expressed in terms of the density ρ_0. The rotational velocity for the power-law models is given by:
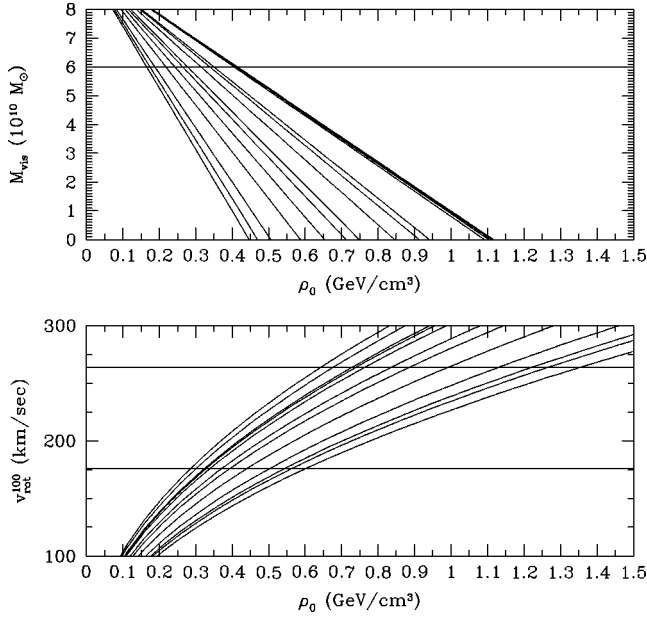
FIG. 1. The quantities M_{vis} (upper panel) and $v_{rot}^{100} \equiv v_{rot}(R = 100$ kpc) (lower panel) calculated as a function of ρ_0 for the halo models summarized in Table II and for $v_0 = 220$ km sec^{-1}. The different curves correspond, from left to right, to the following halo models: A4, A0, D3, A3, A6, A1, A5, D1, A7, C1, C4, C3, A2, C2 (upper panel); A3, A0, D3, A5, A1, A6, A2, A4, C3, A7, C2, C1 (lower panel: here C4 and D1 are not plotted because they are indistinguishable from A7). The horizontal lines indicate the constraints discussed in Sec. IV. The B1–7 models have the same density distribution of the corresponding A1–7 models. D2 and D4 have the same distribution as D1 and D3, respectively.

$$v_{rot}^2 = \frac{\beta \Psi_a R_c^\beta r^2}{(R_c^2 + r^2)^{(\beta+2)/2}}, \tag{25}$$
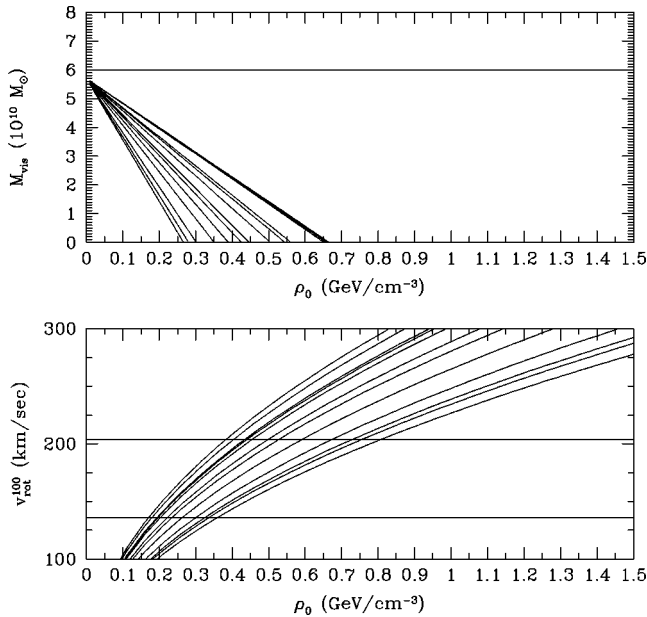
FIG. 2. The same as in Fig. 1 for $v_0 = 170$ km sec^{-1} (the ordering of all the different curves is maintained).
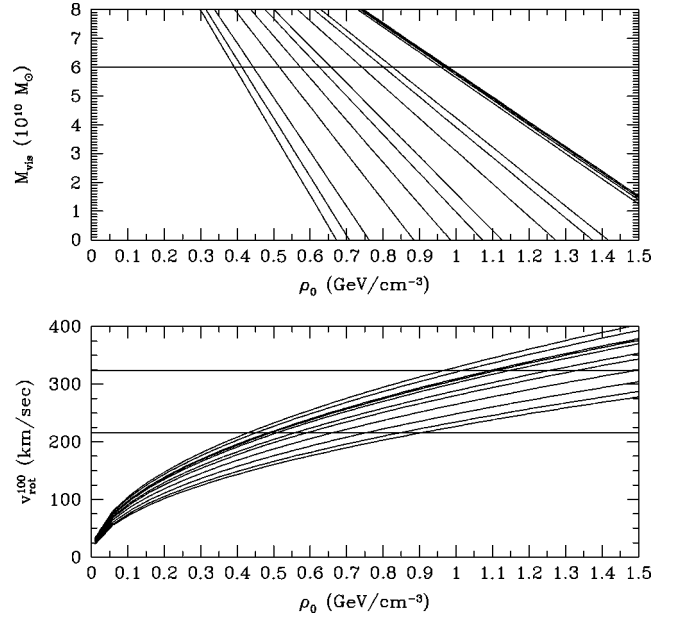
FIG. 3. The same as in Fig. 1 with $v_0 = 270$ km sec^{-1} (the ordering of all the different curves is maintained).

and it is asymptotically falling with r if $\beta > 0$ (model A2) and rising if $\beta < 0$ (model A3).

The last family of spherical models we consider (models A4–A7) is defined by the following matter density:

$$\rho_{DM} = \rho_0 \left(\frac{R_0}{r}\right)^\gamma \left[\frac{1 + (R_0/a)^\alpha}{1 + (r/a)^\alpha}\right]^{(\beta-\gamma)/\alpha} \tag{26}$$

for the choice of values of the parameters α, β, γ and a summarized in Table I. Except for the Jaffe model (A4), the other three density profiles (A5, A6, A7) are obtained from numerical simulations of galaxy evolution.

B. Spherically symmetric matter density with nonisotropic velocity dispersion

The procedure described in the previous section can be generalized to the case of a nonisotropic velocity distribution, while keeping a spherically symmetric density profile. In this case, the most general DF is a function of ϵ and of the
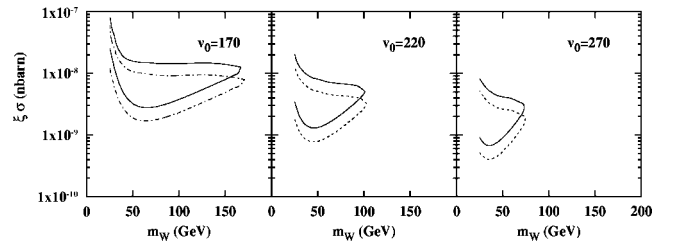

FIG. 4. Plot of the 3σ annual-modulation region in the plane $\xi\sigma_{scalar}^{(nucleon)}$ versus m_W using for the velocity distribution of WIMPs the isothermal sphere model (model A0, see Table II). The three panels of the figure correspond to $v_0 = 170, 220, 270$ km sec^{-1} from left to right. Upper (lower) regions correspond to $\rho_0 = \rho_0^{min}$ (ρ_0^{max}) where ρ_0^{min} and ρ_0^{max} are given in Table III.
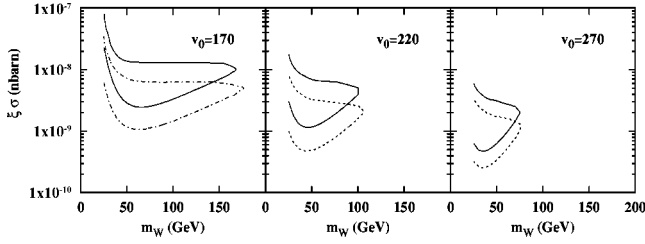
FIG. 5. The same as in Fig. 4 for the velocity distribution of model A1 (see Table II).

magnitude of the angular momentum vector ($L=|\vec{L}|$): $F=F(\epsilon,L)$. Among the different choices which can be performed, a particularly simple case is obtained when F depends on ϵ and L only through the so called Osipkov-Merrit variable [23,11]:

$$Q=\epsilon-\frac{L^2}{2r_a^2}, \tag{27}$$

where the parameter r_a is related to the degree of anisotropy β_0 of the velocity dispersion tensor (evaluated at the Earth's position) in the following way [23]:

$$\beta_0=1-\frac{\bar{v}_\phi^2}{\bar{v}_r^2}=\frac{R_0^2}{R_0^2+r_a^2}. \tag{28}$$

Here the velocity is expressed in spherical coordinates and $\bar{v}_\phi=\bar{v}_\theta\neq\bar{v}_r$ (with $\bar{v}_i^2\equiv\langle v_i^2\rangle-\langle v_i\rangle^2, i=r,\theta,\phi$).

The corresponding DF can be obtained by solving a modified version of Eddington's inversion formula, which is obtained by making the following substitutions in Eq. (13) [11]:

$$\epsilon\to Q, \tag{29}$$

$$\rho_{DM}(r)\to\rho_{Q,DM}(r)\equiv\left(1+\frac{r^2}{r_a^2}\right)\rho_{DM}(r). \tag{30}$$

The models we consider are the same as discussed in Sec. III A: the logarithmic model of Eq. (18) (model B1), the power-law models of Eq. (23) (models B2 and B3) and the models defined by Eq. (26) (models B4–B7). The velocity distribution functions, which are obtained by solving the Eddington equation with the Osipkov-Merrit term, are therefore anisotropic with a degree of anisotropy controlled by the parameter β_0 related to r_a as in Eq. (28).
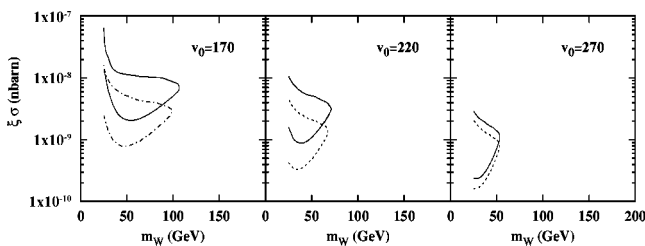
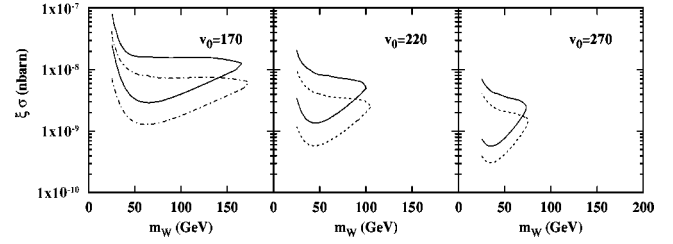FIG. 6. The same as in Fig. 4 for the velocity distribution of model A2.

FIG. 7. The same as in Fig. 4 for the velocity distribution of model A3.

C. Axisymmetric models

In the case of axial symmetry the DF depends in general (at least) on two integrals of motion, the relative binding energy ϵ and the component L_z of the angular momentum along the axis of symmetry. The DF may be written quite generally as the sum of an even (F_+) and an odd (F_-) contribution with respect to L_z:

$$F(\epsilon,L_z)=F_+(\epsilon,L_z)+F_-(\epsilon,L_z), \tag{31}$$

where

$$F_\pm=\frac{1}{2}[F(\epsilon,L_z)\pm F(\epsilon,-L_z)]. \tag{32}$$

When Eq. (12) is extended to the axisymmetric case, the density ρ_{DM} turns out to depend only on the even part F_+ [11], so that, by inverting it, the DF may be determined up to an arbitrary odd part F_-. The problem of the determination of F_+ for an axisymmetric matter density is both analytically and numerically hard to perform and actually it requires a double Laplace inversion on Eq. (12). However, for particular families of axisymmetric potentials this problem has been solved analytically by Evans [16,15]. These families are the axisymmetric generalization of the first two classes already introduced in Sec. III A: the first family has a logarithmic potential, the second one has a power-law potential. We stress that these analytic solutions for F_+ are obtained under the assumption that the halo potential is dominant over the other components. Therefore these solutions correspond to a maximal halo. Even though they do not represent the most general situation, their simplicity makes them of practical use and convenient for studying the axisymmetric case.

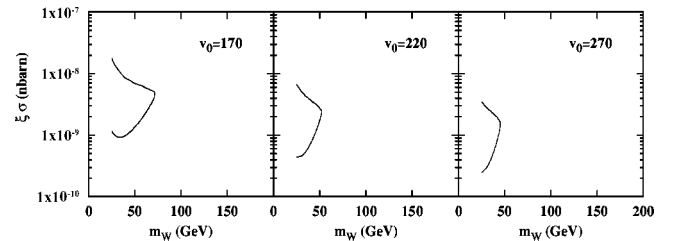The first family of axisymmetric potential we consider is the *logarithmic potential* [15] (models C1 and C2):

FIG. 8. The same as in Fig. 4 for the velocity distribution of model A4. In this case $\rho_0^{max}\simeq\rho_0^{min}$, so upper and lower curves are not distinguishable.
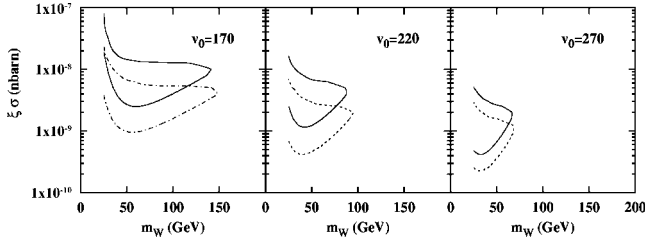
FIG. 9. The same as in Fig. 4 for the velocity distribution of model A5.

$$\Psi_0(R,z) = -\frac{v_0^2}{2}\ln\left(R_c^2 + R^2 + \frac{z^2}{q^2}\right),\qquad (33)$$

where $R^2 = x^2 + y^2$ is the radial coordinate along the galactic plane, R_c is the core radius and q the flatness parameter. The corresponding DM density is

$$\rho_{DM}(R,z) = \frac{v_0^2}{4\pi G q^2}\frac{(2q^2+1)R_c^2 + R^2 + (2-q^{-2})z^2}{(R_c^2 + R^2 + z^2 q^{-2})^2}.\qquad (34)$$

Equations (33) and (34) are the axisymmetric generalization of Eqs. (19) and (18). The corresponding rotational curve is obtained from Eq. (22) by substituting the radial coordinate r with the radial coordinate in the galactic plane R.

By expressing z as a function of Ψ through Eq. (33), the density of Eq. (34) may be decomposed as [16]:

$$\rho = \rho_0(\Psi) + R^2 \rho_1(\Psi),\qquad (35)$$

which allows to determine F_+ in the form:

$$F_+(\epsilon,L_z) = F_+^0(\epsilon) + L_z^2 F_+^1(\epsilon),\qquad (36)$$

leading to a particularly simple analytic solution for the DF [15]. We give it for completeness in Appendix A. The relation of Eq. (35) is no longer valid for a nonmaximal halo, since in that case, the change of variable from z to Ψ is not determined by the potential of Eq. (33) but by an axisymmetric analogous of Eq. (17). Therefore the analytic expression given by Eq. (36) can be used only for maximal halos, i.e. $\rho_0 = \rho_0^{max}$.

The second family of distribution functions is a generalization of the axisymmetric logarithmic potential to the case of an asymptotically nonflat rotational curve, while preserv-
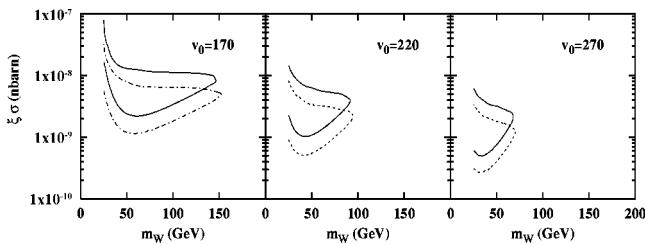

FIG. 10. The same as in Fig. 4 for the velocity distribution of model A6.
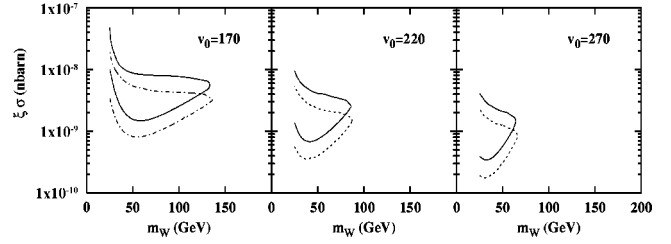

FIG. 11. The same as in Fig. 4 for the velocity distribution of model A7.

ing the property of Eq. (35). This is obtained for the axisymmetric *power-law potential* [16] (models C3 and C4):

$$\Psi_0(R,z) = \frac{\Psi_a R_c^\beta}{(R_c^2 + R^2 + z^2 q^{-2})^{\beta/2}}\quad (\beta\neq 0).\qquad (37)$$

The corresponding matter density is:

$$\rho_{DM}(R,z)$$
$$= \frac{\beta\Psi_a R_c^\beta}{4\pi G q^2}$$
$$\times\frac{(2q^2+1)R_c^2 + (1-\beta q^2)R^2 + [2-q^{-2}(1+\beta)]z^2}{(R_c^2 + R^2 + z^2 q^{-2})^{(\beta+4)/2}}.\qquad (38)$$

Evaluating Eq. (38) for $R=R_0, z=0$ the parameter Ψ_a can be expressed in terms of the density ρ_0. Equations (37) and (38) are the axisymmetric generalization of Eqs. (24) and (23) and they possess the same properties already discussed in Sec. III A. As for the case of the logarithmic potential, the rotational curve is obtained from Eq. (25) by substituting the radial coordinate r in Eq. (25) with the radial coordinate in the galactic plane R, and it is asymptotically falling with R if $\beta>0$ (model C3) and rising if $\beta<0$ (model C4).

In analogy with the logarithmic case, also for the power-law model an analytic solution for the DF can be worked out [16] with the form of Eq. (36). This applies again only for a maximal halo. The analytic formulas for F_+ can be found for completeness in Appendix A.
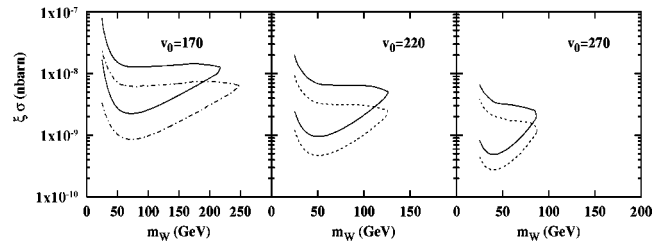

FIG. 12. The same as in Fig. 5, with anisotropy of the velocity dispersion through the Osipkov-Merrit term and anisotropy parameter $\beta_0 = 0.4$ (model B1). The horizontal axis has been extended in the first panel.
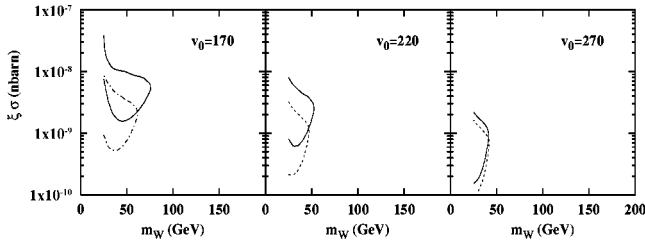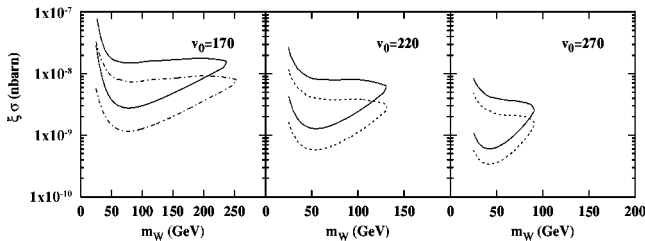
FIG. 13. The same as in Fig. 6, with anisotropy of the velocity dispersion through the Osipkov-Merrit term and anisotropy parameter $\beta_0 = 0.4$ (model B2).

Co-rotation and counter-rotation of the halo

As mentioned before, the DF for an axisymmetric model is known up to an arbitrary odd component F_-. The DF we summarized above for the Evan's models all refer to the pure even component: they all have $F_-(\epsilon, L_Z) = 0$ and possess no bulk rotation. The case $F_-(\epsilon, L_Z) \neq 0$ corresponds to the case of a rotating halo, where the number of particles moving clockwise around the axis of symmetry is different from that in the opposite sense.

A family of DF's with bulk rotation can be studied by constructing an explicit example for F_-. This can be done, starting from a generic F_+, by considering the linear combination [24–26]:

$$F_-(\epsilon, L_z) = F_{right}(\epsilon, L_z) - F_{left}(\epsilon, L_z), \qquad (39)$$

where

$$F_{right}(\epsilon, L_z) = \begin{cases} F_+(\epsilon, L_z), & v_\phi > 0, \\ 0, & v_\phi < 0, \end{cases} \qquad (40)$$

and

$$F_{left}(\epsilon, L_z) = \begin{cases} 0, & v_\phi > 0, \\ F_+(\epsilon, L_z), & v_\phi < 0. \end{cases} \qquad (41)$$

The distributions F_{right} and F_{left} describe the configurations with maximal $|\bar{v}_\phi|$ with the same density profile as F_+ [24]. A DF with an intermediate value of $\bar{v}_\phi$ can be obtained as a linear combination of F_+ and F_-, or, equivalently, of F_{left} and F_{right}:

$$F(\epsilon, L_z) = \eta F_{right}(\epsilon, L_z) + (1 - \eta) F_{left}(\epsilon, L_z). \qquad (42)$$

FIG. 14. The same as in Fig. 7, with anisotropy of the velocity dispersion through the Osipkov-Merrit term and anisotropy parameter $\beta_0 = 0.4$ (model B3). The horizontal axis has been extended in the first panel.
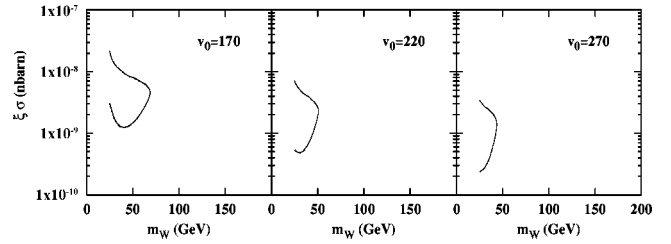

FIG. 15. The same as in Fig. 8, with anisotropy of the velocity dispersion through the Osipkov-Merrit term and anisotropy parameter $\beta_0 = 0.4$ (model B4). In this case $\rho_0^{max} \simeq \rho_0^{min}$, so upper and lower curves are not distinguishable.

The parameter η ranges from 1 (maximal co-rotation) to 0 (maximal counter-rotation) and is related to the dimensionless spin parameter λ of the Galaxy by: $\lambda = 0.36|\eta - 0.5|$ [25]. In order to be consistent with the available extensive numerical work on galaxy formation, λ should not exceed the value 0.05 [27], implying $0.36 \lesssim \eta \lesssim 0.64$. For all the Evans model discussed in this section, we will also study the co- and counter-rotating situations, adopting the two values $\eta = 0.36$ and $\eta = 0.64$.

D. Triaxial models

The last class of models we wish to discuss is represented by the *triaxial potential* discussed in Ref. [17]:

$$\Psi_0(x, y, z) = -\frac{1}{2} v_0^2 \ln\left(x^2 + \frac{y^2}{p^2} + \frac{z^2}{q^2} \right), \qquad (43)$$

which, for a maximal halo, corresponds to the DM density:

$$\rho_{DM}(x, y, z) = \frac{v_0^2}{4\pi G} \frac{Ax^2 + By^2/p^2 + Cz^2/q^2}{(x^2 + y^2/p^2 + z^2/q^2)^2} \qquad (44)$$

where $A = p^{-2} + q^{-2} - 1, B = 1 + q^{-2} - p^{-2}$ and $C = 1 + p^{-2} - q^{-2}$. In Ref. [17] the velocity DF $f(\vec{v})$ of the system is approximated by a triaxial Gaussian with semiaxes equal to the velocity dispersions as obtained by the solutions of the Jeans equations:

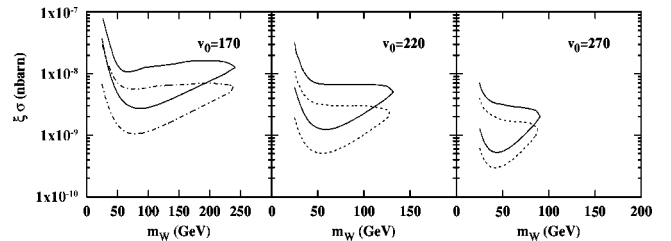$$\bar{v}_r^2 = \frac{v_0^2}{(2 + \delta)(p^{-2} + q^{-2} - 1)} \qquad (45)$$
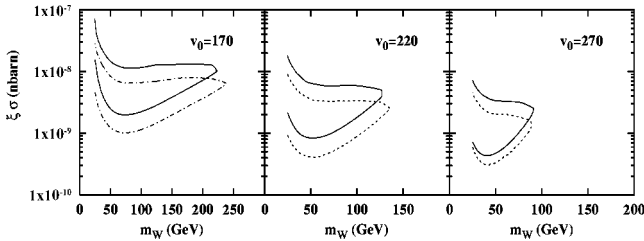

FIG. 16. The same as in Fig. 9, with anisotropy of the velocity dispersion through the Osipkov-Merrit term and anisotropy parameter $\beta_0 = 0.4$ (model B5). The horizontal axis has been extended in the first panel.

TABLE III. Allowed intervals of ρ_0 obtained from the constraints on M_{vis} and v_{rot}^{100} for the halo models summarized in Table II. The values of ρ_0^{max} and ρ_0^{min} are used in the modulation analysis of the experimental data of Figs. 4–18 for the models of class A and B, while only ρ_0^{max} is used for models of class C and D in Figs. 19–34. The value of ρ_0^{max} for the axisymmetric models of class C is not affected by the inclusion of a co-rotation or counter-rotation effect through Eq. (42).

| Model | $v_0 = 170$ km sec^{-1} | | $v_0 = 220$ km sec^{-1} | | $v_0 = 270$ km sec^{-1} | |
	ρ_0^{min}	ρ_0^{max}	ρ_0^{min}	ρ_0^{max}	ρ_0^{min}	ρ_0^{max}
A0	0.18	0.28	0.30	0.47	0.45	0.71
A1,B1	0.20	0.42	0.34	0.71	0.62	1.07
A2,B2	0.24	0.53	0.41	0.89	0.97	1.33
A3,B3	0.17	0.35	0.29	0.59	0.52	0.88
A4,B4	0.26	0.27	0.44	0.45	0.66	0.67
A5,B5	0.20	0.44	0.33	0.74	0.66	1.11
A6,B6	0.22	0.39	0.37	0.65	0.57	0.98
A7,B7	0.32	0.54	0.54	0.91	0.82	1.37
C1	0.36	0.56	0.60	0.94	0.91	1.42
C2	0.34	0.67	0.56	1.11	0.98	1.68
C3	0.30	0.66	0.50	1.10	0.97	1.66
C4	0.32	0.65	0.54	1.09	0.96	1.64
D1,D2	0.32	0.50	0.54	0.84	0.81	1.27
D3,D4	0.19	0.30	0.32	0.51	0.49	0.76

$$\bar{v}_\phi^2 = \frac{v_0^2(2q^{-2}-1)}{2(p^{-2}+q^{-2}-1)} \tag{46}$$

$$\bar{v}_\theta^2 = \frac{v_0^2(2p^{-2}-1)}{2(p^{-2}+q^{-2}-1)} \tag{47}$$

when the Earth's position is on the major axis of the equipotential ellipsoid (models D1 and D2), and:

$$\bar{v}_r^2 = \frac{v_0^2 p^{-4}}{(2+\delta)(1+q^{-2}-p^{-2})} \tag{48}$$

$$\bar{v}_\phi^2 = \frac{v_0^2(2q^{-2}-p^{-2})}{2(1+q^{-2}-p^{-2})} \tag{49}$$

$$\bar{v}_\theta^2 = \frac{v_0^2(2-p^{-2})}{2(1+q^{-2}-p^{-2})} \tag{50}$$

when the Earth's position is on the intermediate axis (models D3 and D4). In Eqs. (45), (48) the quantity δ is a free parameter that in the spherical limit ($p=q=1$) quantifies the degree of anisotropy of the velocity dispersion tensor:

$$\frac{\bar{v}_\phi^2}{\bar{v}_r^2} = \frac{2+\delta}{2}. \tag{51}$$

IV. CONSTRAINING THE MODELS

Once a given model is chosen for the velocity distribution function of the dark matter particles, the parameters of the model have to be fixed using observational data. Unfortunately, due to its "darkness," all our knowledge of the halo is of indirect nature [28,22] and it includes requirements on the circular rotational speed (constraints on its flatness and its value at the solar circle and in the outer regions of the Galaxy) as well as observational constraints on the local surface density of the disk and on the dispersion velocity of the bulge. In general, one should construct a composite model of the Galaxy where the DM is coupled to other components
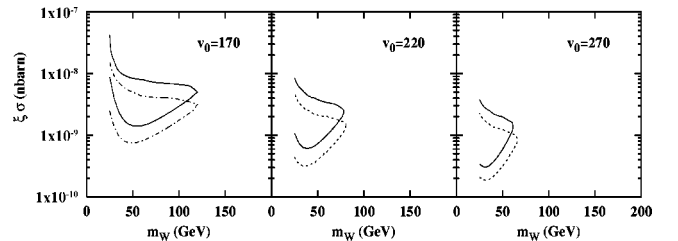

FIG. 17. The same as in Fig. 10, with anisotropy of the velocity dispersion through the Osipkov-Merrit term and anisotropy parameter $\beta_0 = 0.4$ (model B6). The horizontal axis has been extended in the first panel.

FIG. 18. The same as in Fig. 11, with anisotropy of the velocity dispersion through the Osipkov-Merrit term and anisotropy parameter $\beta_0 = 0.4$ (model B7).
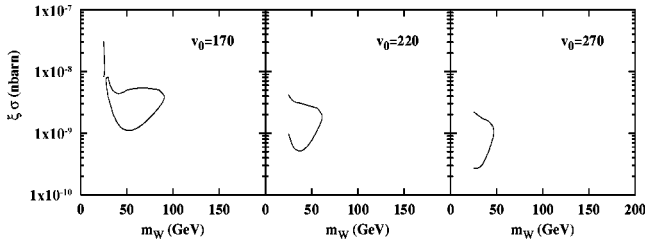
FIG. 19. The same as in Fig. 4 for the velocity distribution of model C1. Only the case $\rho_0=\rho_0^{max}$ is shown.

like the disk and the bulge, and the parameters describing the various components are varied independently requiring that the observational constraints are satisfied.

We have already noticed that WIMP direct detection rates are particularly sensitive to the value of the rotational velocity v_0 and the local DM density ρ_0 (both evaluated at the solar circle). The procedure we follow in order to determine the allowed ranges for v_0 and ρ_0 in each galactic model is explained in the following. First of all, the experimental information we use is: the allowed range for the local rotational velocity, the amount of flatness of the rotational curve of our Galaxy and the maximal amount of nonhalo components in the Galaxy. The first information directly fixes the allowed interval for v_0, irrespective of the galactic halo model. The other constraints are used in order to determine the allowed ranges for ρ_0, for each halo model.

The allowed interval for v_0 is:

$$v_0=(220\pm50)\ \text{km sec}^{-1}\quad(90\%\ \text{C.L.}),\qquad(52)$$

which conservatively relies on purely dynamical observations [29]. Proper motion measurements of nearby stars [30] lead to similar estimates for the central value of v_0, with a significantly smaller uncertainty. However they are based on the assumption of circular orbit of the observed objects. For definiteness, we will use in the following three representative values for v_0, which correspond to its central value and to the boundaries of its allowed 90% C.L. range of Eq. (52): $v_0=170,220,270\ \text{km sec}^{-1}$.

For the three representative values of v_0 we then determine the corresponding allowed ranges for ρ_0. For each halo model and for each value of v_0, we calculate, as a function of ρ_0, two quantities: (i) the total amount of mass M_{vis} in components other than the halo (e.g.: disk, bulge) which is necessary in order to match the given value of local rotational
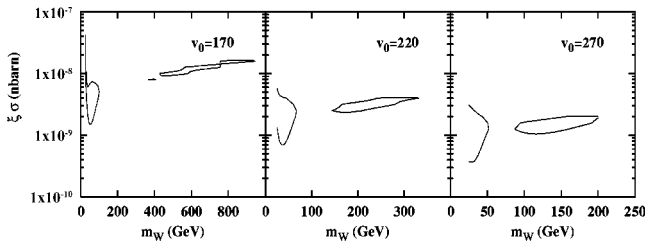

FIG. 20. The same as in Fig. 19 including a co-rotation effect of the halo with $\eta=0.64$. The horizontal axis has been extended in all panels.
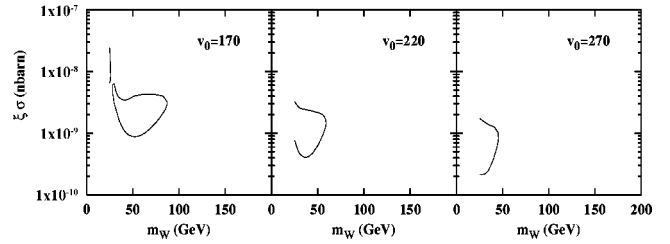
velocity v_0; (ii) the value of the rotational curve at a distance of 100 kpc from the center of the Galaxy: $v_{rot}^{100}\equiv v_{rot}$ ($R=100$ kpc). These two quantities are somewhat constrained from observations, even though their constraints are often obtained by using some degree of galactic modeling. We conservatively quote the following ranges [22,28]:

$$1\times10^{10}M_\odot\lesssim M_{vis}\lesssim6\times10^{10}M_\odot\qquad(53)$$

$$0.8\cdot v_0\lesssim v_{rot}^{100}\lesssim1.2\cdot v_0,\qquad(54)$$

where $M_\odot$ denotes the solar mass. The first constraint limits the amount of nonhalo components, while the second is a constraint of "essentially flatness" rotational curve: only galactic halo models which provide a rotational curve which does not deviate from a flat one more than 20% at 100 kpc are accepted. The constraint of Eq. (54) is compatible with the estimates of the galactic mass at large radii as obtained by the dynamics of satellites of the Galaxy [22].

The behavior of M_{vis} and v_{rot}^{100} as a function of ρ_0 is shown in Fig. 1 (which refers to $v_0=220$ km s^{-1}), Fig. 2 ($v_0=170$ km s^{-1}), and Fig. 3 ($v_0=270$ km s^{-1}). Each line refers to a different halo model. The upper panels show that M_{vis} is a decreasing function of ρ_0, since increasing the amount of dark matter in the Galaxy implies that less matter in other galactic components is required to support the rotational curve. On the other hand, the value of the rotational velocity in the outer Galaxy is totally supported by the dark halo, and it is larger for more massive halos.

When the constraints expressed in Eqs. (53) and (54) are simultaneously applied, an allowed interval for ρ_0 may be derived for each halo model.

The procedure outlined above may be used as a simple recipe for identifying the intervals for the local density parameter. However, some caution must be taken in the application of the bounds on M_{vis} in Eq. (53). As already dis-

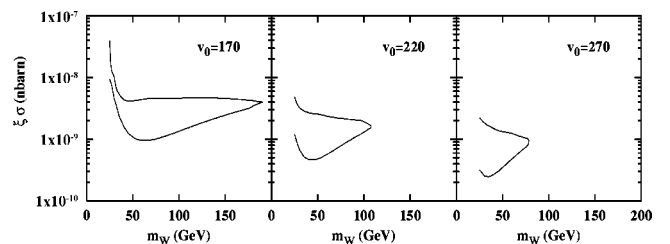FIG. 21. The same as in Fig. 19 including a counter-rotation effect of the halo with $\eta=0.36$.

FIG. 22. The same as in Fig. 4 for the velocity distribution of model C2. Only the case $\rho_0=\rho_0^{max}$ is shown.
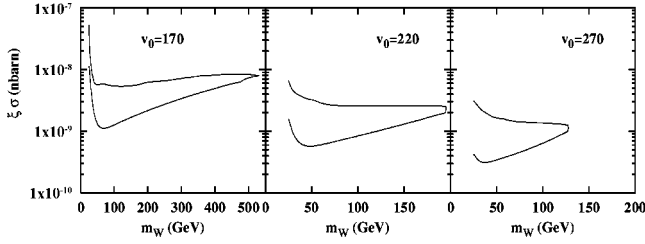
FIG. 23. The same as in Fig. 22 including a co-rotation effect of the halo with $\eta = 0.64$. The horizontal axis has been extended in the first panel.

cussed in the previous section, for the models of class A and class B we solve the Eddington equation in order to determine the velocity distribution function of dark matter particles. In this case we can take into account also the situation in which the local rotational velocity is only partially supported by the halo, and therefore we can apply the limits to M_{vis} given by Eq. (53). Instead, the analytic models of class C and class D may be applied only to the extreme case of a fully maximal-halo, since the analytic formulas for $f(\vec{v})$ are derived under the assumption that only the halo matter density is present. For these models (class C and class D) the only case we can deal with is that of a fully maximal halo, which corresponds to $M_{vis} = 0$. This represents a conservative upper limit for ρ_0. From Figs. 1–3 we can see that the upper bounds to ρ_0 obtained from the $M_{vis} = 0$ limit are only a few percent larger than what is obtained by imposing the lower limit of Eq. (53): $M_{vis} = 1 \times 10^{10} M_\odot$. For consistency and simplicity, we will use $M_{vis} \simeq 0$ as a lower limit also for models of class A and B.

The allowed intervals for ρ_0 that we obtain by imposing the bounds on M_{vis} and v_{rot}^{100} are listed in Table III. As discussed above, both values ρ_0^{min} and ρ_0^{max} will be used in the next sections to perform the modulation analysis of the DAMA-NaI experimental data, while only ρ_0^{max} will be used for the analysis of the data for models of class C and D. We stress that the reason for this stands in the fact that for the analytic models of classes C and D, we know $f(\vec{v})$ only for a maximal–halo.

V. RESULTS AND DISCUSSION

In this section we make use of the halo models described in Sec. III, with the choice of parameters shown in Table II, to analyze the annual-modulation signal present in the
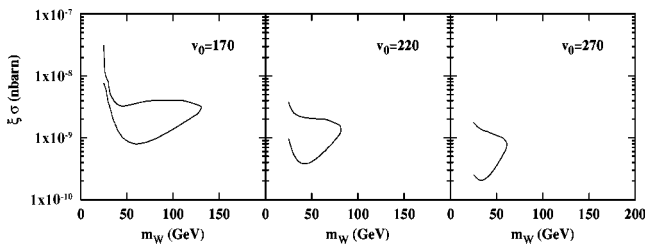

FIG. 24. The same as in Fig. 22 including a counter-rotation effect of the halo with $\eta = 0.36$.
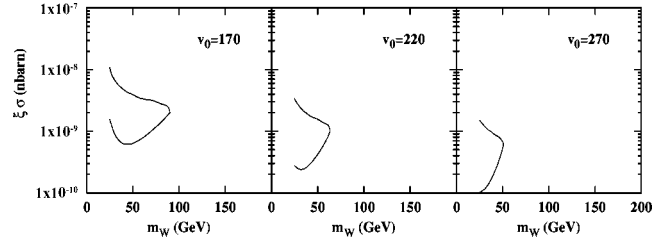

FIG. 25. The same as in Fig. 4 for the velocity distribution of model C3. Only the case $\rho_0 = \rho_0^{max}$ is shown.

DAMA-NaI data [2] in terms of relic WIMPs with purely coherent interactions. The procedure is the one outlined in Sec. II. The results are presented as 3σ annual-modulation regions shown in the plane $\xi\sigma_{scalar}^{(nucleon)}$ versus m_W. All figures are divided in three panels which correspond to the cases: $v_0 = 170, 220, 270$ km sec^{-1}.

A general feature of all the models is that by raising the parameter v_0 the modulation region moves from the upper-right to the lower-left of the m_W-$\xi\sigma_{scalar}^{(nucleon)}$ plane. This is easily understood since, for a given DM density profile, higher values of v_0 imply higher values of ρ_0 [through Eq. (2)] and of the velocity ellipsoid $\sigma_{ij} \equiv \langle v_i v_j \rangle$ (through the Jeans equations); the experimental value of the signal and the measured WIMP-nucleus recoil energy are fixed by the data, therefore the modulation region moves downward because

$$\frac{dR_{det}}{dE_R} \propto \rho_0 \times \sigma_{scalar}^{(nucleon)} \qquad (55)$$

[see Eq. (6)] and moves to lower masses because

$$E_R \propto m_W \times \langle v^2 \rangle. \qquad (56)$$

On the other hand, when one compares the different density profiles that we have discussed in the previous sections, it is worth noticing that, for a given value of v_0, a stronger singularity in the galactic center lowers the value of ρ_0^{max} (in order to keep constant the mass integral) with the consequence that the lower part of the modulation region rises. So the smallest values of $\xi\sigma_{scalar}^{(nucleon)}$ are reached by the models with a less singular density profile.

Figures 4–18 show the result of the analysis for the models with a spherically symmetric density profile (models A0–7, B1–7). Models A0–7 have an isotropic velocity dispersion, while in models B1–7 a degree of anisotropy in the velocity dispersion is introduced through the Osipkov-Merrit
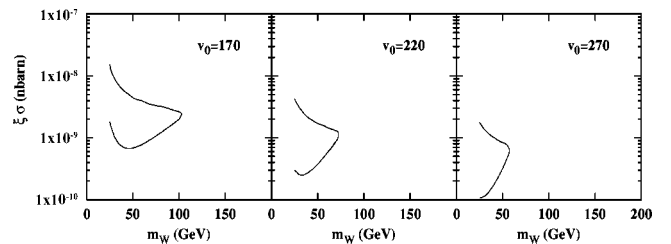

FIG. 26. The same as in Fig. 25 including a co-rotation effect of the halo with $\eta = 0.64$.
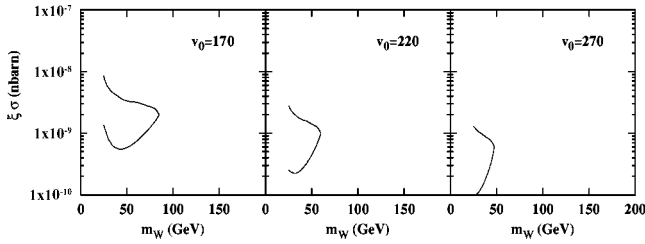
FIG. 27. The same as in Fig. 25 including a counter-rotation effect of the halo with $\eta = 0.36$.

FIG. 29. The same as in Fig. 28 including a co-rotation effect of the halo with $\eta = 0.64$.

term of Eq. (27). The amount of anisotropy is controlled by the β_0 parameter of Eq. (28) and it has been fixed at the value: $\beta_0 = 0.4$. This value corresponds to a radial anisotropy. In order to account for the uncertainty in the DM local density ρ_0, for each case two regions are given, the higher (lower) corresponding to $\rho_0 = \rho_0^{min}$ (ρ_0^{max}), where ρ_0^{min} and ρ_0^{max} have been obtained as discussed in Sec. IV and are reported in Table III. The numerical values of the parameters summarized in the third column of Table II have been chosen in order to ensure the compatibility of the curves of Figs. 1, 2, 3 with the constraints of Eqs. (53), (54), discussed in Sec. IV. The Jaffe models A4, B4, which go into the isothermal sphere when $R_c \rightarrow \infty$, have been calculated for the smallest allowed value of the core radius R_c in order to examine the case of maximal departure from the usual scenario. As a consequence of this, for this model $\rho_0^{min} \simeq \rho_0^{max}$ and in Figs. 8,15 the upper and lower modulation regions are superimposed.

The effect of radial anisotropy in the velocity dispersion tensor ($\bar{v}_r > \bar{v}_\theta = \bar{v}_\phi$), which occurs for the models of class B, may be seen by comparing Figs. 5–11 with the corresponding Figs. 12–18. As a general feature, a reduction of the modulation effect is expected, since the WIMPs phase space is depopulated along the direction of the Sun's velocity. This is confirmed by the fact that in most cases the modulation regions move upwards and widen, although the size of the effect can be small. The effect of radial anisotropy on the WIMP mass is more involved. In particular, the modulation regions for models B1, B3, B5, B6 extend to heavier WIMP masses compared to the corresponding isotropic cases, while for models B2, B4, B7 the region moves to smaller WIMP masses.

As already pointed out, for the models belonging to classes C and D only the regions for $\rho_0 = \rho_0^{max}$ are shown. As far as the axisymmetric models of class C are concerned,
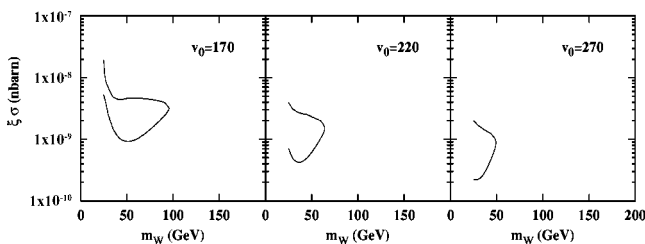
they are shown in Figs. 19, 22, 25, 28. In each model the flatness parameter q has been chosen in order to have the maximal flatness compatible with observations and with the positivity of the DF. The main effect induced by flatness is through the increase in the local density ρ_0, as can be seen in Table III. As a consequence, the modulation regions for these models reach values of $\xi\sigma_{scalar}^{(nucleon)}$ significantly below the levels of the spherical cases. In Figs. 20, 23, 26, 29 the same models are shown with a co-rotation effect of the halo implemented through Eq. (42) with $\eta = 0.64$, while in Figs. 21, 24, 27, 30 for the same models a counter-rotation effect with $\eta = 0.36$ has been introduced. The main consequence of halo co-rotation is a decrease of the relative velocity between WIMPs and the Earth. The energy of WIMPs is therefore smaller and in order to produce the same recoil energy in the detector the WIMPs have to be heavier. This can be verified in the figures, where the modulation region of co-rotating models may reach very high WIMP masses, even higher than 200 GeV. By the same token, in counter-rotating models the modulation region is shifted toward lower masses.

The peculiar shape of the modulation region of Fig. 20 deserves some comments. The two disconnected closed contours, which arise at different m_W values, are indicative of the superposition in the WIMP phase space of two components with well separated r.m.s. velocities. This is exemplified in Fig. 35 for the models B1 ($q=1$) and C1 ($q = 1/\sqrt{2}$), where the contour plots of the corresponding DF's are plotted in the v-v_ϕ plane (in the galactic rest frame) and in the w-w_ϕ plane (in the Earth's rest frame). It is evident from the figure that, in flattened models, small $|L_z|$ orbits are depopulated compared to the spherical case, leading to two well separated populations with $v_\phi > 0$ and $v_\phi < 0$. These two components have the same temperature in the galactic rest frame, but develop different r.m.s. velocities when boosted in the Earth's rest frame. As shown in Fig. 35, the relative weight of the two populations can be tilted towards

FIG. 28. The same as in Fig. 4 for the velocity distribution of model C4. Only the case $\rho_0 = \rho_0^{max}$ is shown.
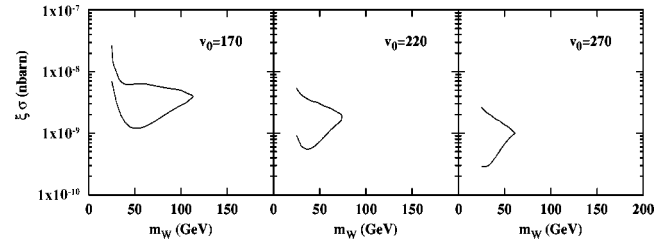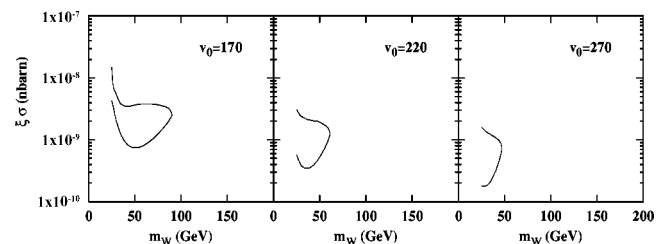

FIG. 30. The same as in Fig. 28 including a counter-rotation effect of the halo with $\eta = 0.36$.

FIG. 31. The same as in Fig. 4 for the velocity distribution of model D1. Only the case $\rho_0 = \rho_0^{max}$ is shown.
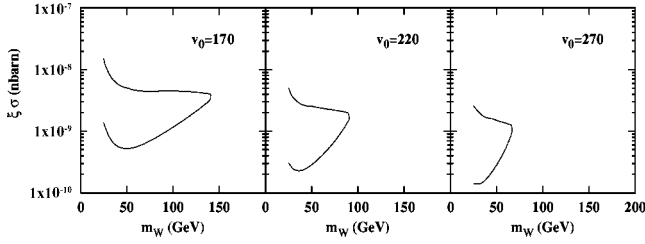

FIG. 33. The same as in Fig. 4 for the velocity distribution of model D3. Only the case $\rho_0 = \rho_0^{max}$ is shown.

slow or fast WIMPs in the two cases of a co-rotating or counter-rotating halo, respectively. This explains why the co-rotating model of Fig. 20 develops a second minimum at high WIMP masses, and this is not observed in the corresponding non-rotating or counter-rotating cases. We have numerically verified that the peculiar disconnected region at high WIMP masses reduces in size when the flatness parameter is increased (since in this way the velocity distribution function becomes more similar to the nonflattened one), while it shifts towards lower masses when the core radius R_c is decreased.

We conclude the discussion of our results with the triaxial models shown in Figs. 31, 32, 33, 34 where, to be definite, the same choice of parameters of Ref. [17] is adopted. For these models a general solution for the DF is not available. Only the velocity ellipsoid of Eqs. (45)–(48) is known, and it is used to fix the second moments of a nonisotropic Maxwellian. This explains why the shape of the modulation regions is quite similar to the standard case. In models D1 and D2 the Earth is assumed to be located on the major axis of the density ellipsoid, while in models D3 and D4 it is placed on the intermediate axis. Since in the two cases the Sun's position R_0 is the same, ρ_0 is higher for models D1, D2 than for models D3, D4 (see Table III). As a consequence, the modulation regions of Figs. 31 and 32 reach smaller values of $\xi\sigma_{scalar}^{(nucleon)}$ compared to those of Figs. 33 and 34. Models D1 and D3 (D2 and D4) have $\delta = -1.78$ ($\delta = 16$), which implies a radial (tangential) anisotropy of the velocity ellipsoid [see Eq. (51)]. Solving the Jeans equation for the potential of Eq. (43) in the spherical limit $q = p = 1$ (which corresponds to a noncored isothermal sphere) leads to the relation [11]

$$v_\phi^2 + v_\theta^2 = \frac{3}{2}v_0^2. \tag{57}$$

Note that this property is a consequence of the flatness of the rotational curve, and would not be true, for instance, including a core radius in the potential. Equation (57) implies that, in this model, the tangential components of the velocity ellipsoid are fixed by v_0. As a consequence of this, radial anisotropy ($v_r > v_\theta = v_\phi$) corresponds to faster WIMPs and tangential anisotropy to slower WIMPs. This shifts the modulation regions towards smaller values of m_W in Figs. 31 and 33 and higher values of m_W in Figs. 32 and 34. This effect is sizeable in the case of tangential anisotropy, where the modulation region may extend up to $m_W \simeq 270$ GeV.

The results of this section are summarized in Fig. 36, where all the modulation regions previously discussed have been plotted jointly. A convolution of all the regions may be indicative of the uncertainties in the determination of the WIMP modulation signal due to the modeling of the WIMP DF. As a final result, we show such a convolution in Fig. 37, where a single curve in the plane m_W-$\xi\sigma_{scalar}^{(nucleon)}$ is plotted by collecting the information contained in the analyses of all the nonrotating models considered in this paper. The region is compared with the original annual modulation region obtained in Ref. [2] for an isothermal sphere model of the galactic halo with rotational velocity $v_0 = 220$ km s^{-1} and local dark matter density $\rho_0 = 0.3$ GeV cm^{-3}. From Fig. 37 we see that the DAMA-NaI annual modulation result is compatible with WIMPs masses up to $m_W \simeq 270$ GeV and WIMP-nucleon cross sections in the interval: 10^{-10} nbarn $\lesssim \xi\sigma_{scalar}^{(nucleon)} \lesssim 6 \times 10^{-8}$ nbarn when the uncertainties in the WIMP velocity DF are taken into account. Co-rotating models with maximal corotation can extend the mass range even further, up to $m_W \simeq 500$–900 GeV, for cross section of the order few$\times 10^{-9}$ nbarn $\lesssim \xi\sigma_{scalar}^{(nucleon)} \lesssim 2 \times 10^{-8}$ nbarn, as it can be seen, for instance, in Fig. 36.
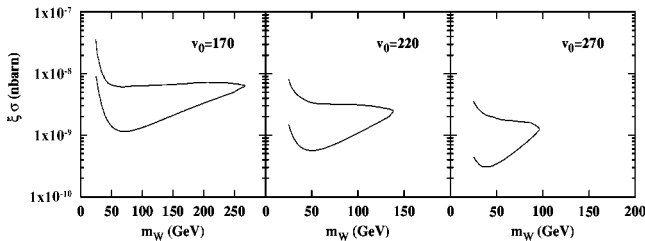

FIG. 32. The same as in Fig. 4 for the velocity distribution of model D2. Only the case $\rho_0 = \rho_0^{max}$ is shown. The horizontal axis has been extended in the first panel.
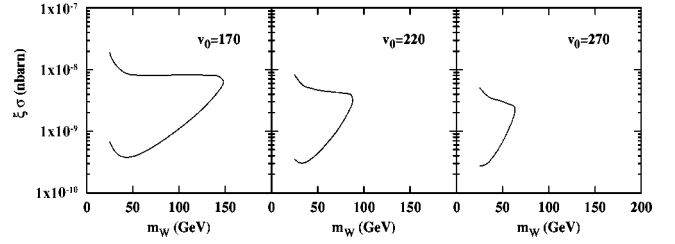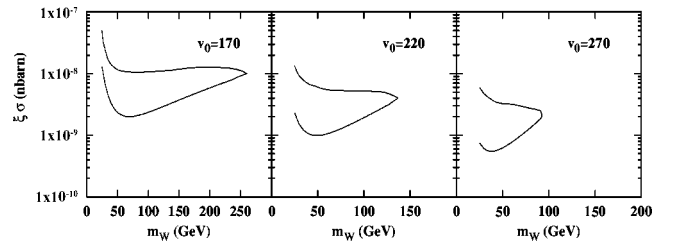

FIG. 34. The same as in Fig. 4 for the velocity distribution of model D4. Only the case $\rho_0 = \rho_0^{max}$ is shown. The horizontal axis has been extended in the first panel.
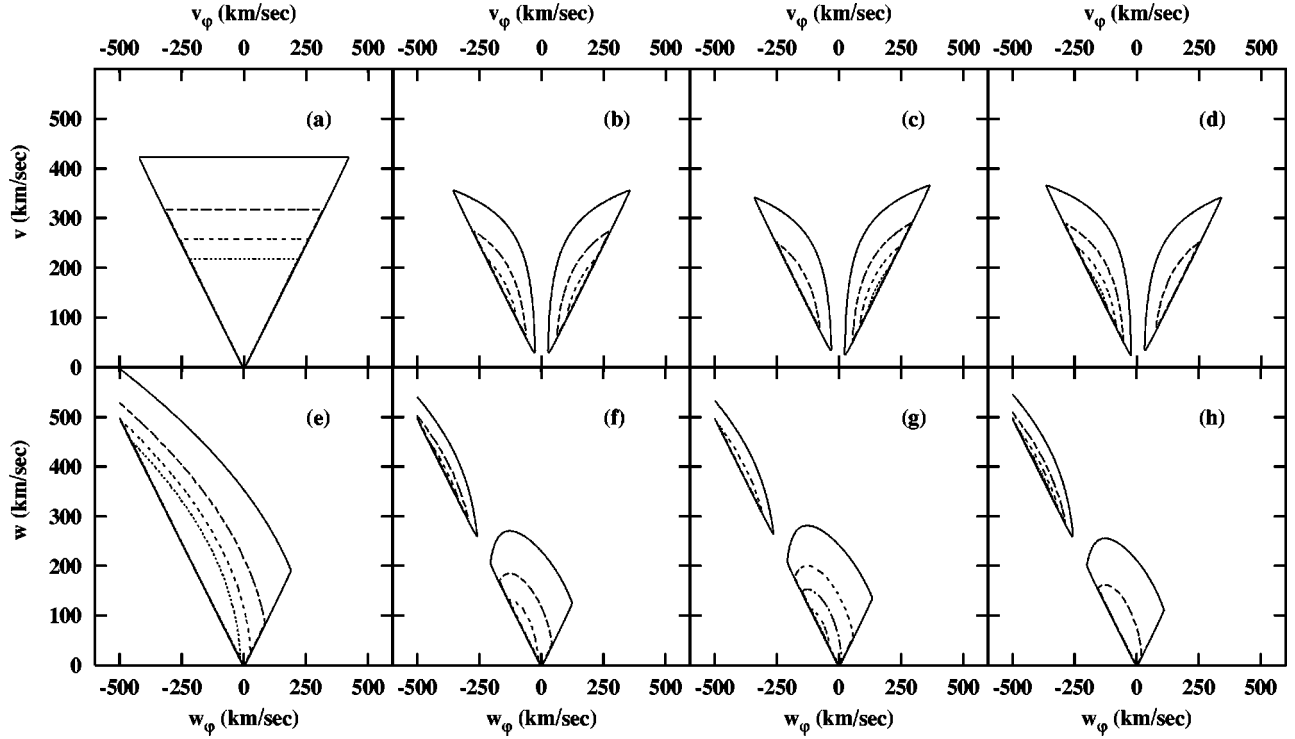
FIG. 35. Contour plots of the DF's for models B1 and C1 (see Table II). From left to right, the different panels refer to models B1 [panels (a) and (e)], C1 [panels (b) and (f)], co-rotating C1 [panels (c) and (g)], counter-rotating C1 [panels (d) and (h)]. Upper panels are plotted in the v_ϕ-v plane, defined in the reference frame of the Galaxy, while lower panels are shown in the w_ϕ-w plane, defined in the reference frame of the Earth. Solid lines, big dashes, small dashes and dots correspond to growing values of the DF (in arbitrary units). The two disconnected closed contours which arise at different w values in panels (f), (g) and (h) signal the superposition in the WIMP phase space of two components with well separated r.m.s. velocities.

VI. CONCLUSIONS

In the present paper we have extended a previous analysis of the DAMA modulation experiment for the case of a WIMP with a purely spin-independent coupling, by discussing in detail the implications on the results of the uncertainties on the dark matter galactic velocity distribution. We have studied a large number of viable models which deviate from the standard isothermal sphere in the matter density profile, in the presence of anisotropies of the velocity dispersion tensor and in effects of rotation of the galactic halo. The different models have been classified according to the symmetry
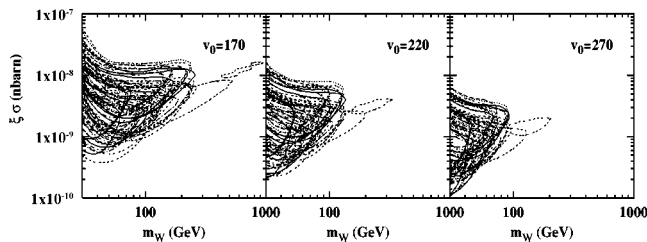

FIG. 36. Summary of the 3σ annual-modulation regions in the plane $\xi\sigma_{\text{scalar}}^{(\text{nucleon})}$ versus m_W, obtained by superimposing the results obtained with the velocity distributions of all the models described in Table II. For each of the models A1–7 and B1–7 two regions are plotted, which refer to the two extreme values ρ_0^{min} and ρ_0^{max} shown in Table III for the WIMP local density ρ_0. For models C1–4 and D1–4 only the regions which refer to $\rho_0 = \rho_0^{max}$ are shown.
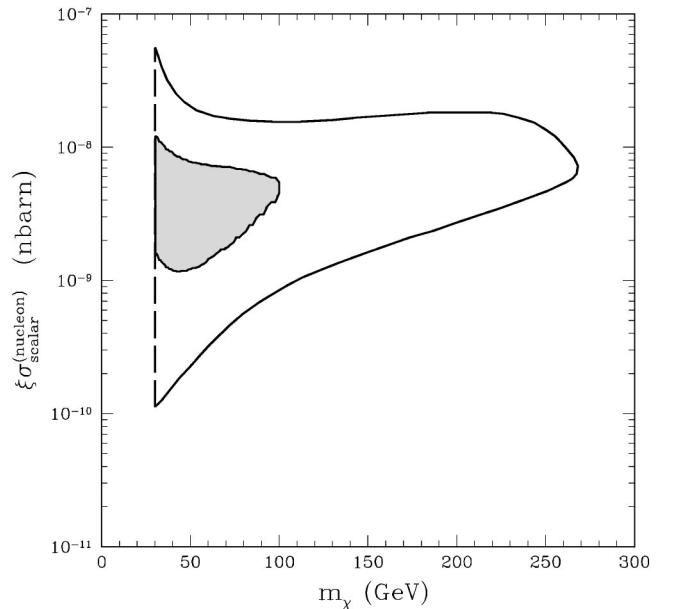

FIG. 37. 3σ annual-modulation region in the plane $\xi\sigma_{\text{scalar}}^{(\text{nucleon})}$ versus m_W, obtained by considering all the (nonrotating) galactic halo models discussed in this paper. The region is compared with the original annual modulation contour (shaded region) obtained in Ref. [2] for an isothermal sphere model of the galactic halo with rotational velocity $v_0 = 220 \text{ km s}^{-1}$ and local dark matter density $\rho_0 = 0.3 \text{ GeV cm}^{-3}$.

properties of their matter density profile (or gravitational potential) and of the velocity distribution function. We have specifically considered: (*a*) spherically symmetric matter density with isotropic velocity dispersion; (*b*) spherically symmetric matter density with nonisotropic velocity dispersion; (*c*) axisymmetric models; (*d*) triaxial models.

The different models have then been used to reanalyze the DAMA-NaI 0–4 data collected by the DAMA-NaI Collaboration [2]; in particular a total exposure of 57986 kg day, which corresponds to 4 annual cycles, has led to the observation of an annual modulation effect. The hypothesis of WIMP annual modulation, already favored in the previous studies [2,4] by using an isothermal sphere, is confirmed in all the investigated scenarios, and the effects of the different halo models on the determination of the allowed maximum-likelihood region in the WIMP mass and WIMP-nucleon cross-section have been derived. We can summarize that the DAMA-NaI annual modulation result is compatible with WIMPs masses up to $m_W \simeq 270$ GeV and WIMP-nucleon cross sections in the interval: 10^{-10} nbarn $\lesssim \xi\sigma_{\text{scalar}}^{(\text{nucleon})} \lesssim 6 \times 10^{-8}$ nbarn, when the uncertainties in the WIMP velocity DF are taken into account. When also co-rotation of the galactic halo is considered, the mass range extends further to $m_W \simeq 500$–900 GeV, for a cross section of the order a few $\times 10^{-9}$ nbarn $\lesssim \xi\sigma_{\text{scalar}}^{(\text{nucleon})} \lesssim 2 \times 10^{-8}$ nbarn. These intervals quantify the extent of the annual modulation region for WIMPs with purely spin-independent couplings, as due to uncertainties in the phase space distribution function of galactic WIMPs.

APPENDIX: AXISYMMETRIC MODELS

In this appendix we give, for completeness, the analytic formulas of the DF's for the axisymmetric potentials of Eqs. (33), (37) adapted from Refs. [15,16]. All expressions are written in the reference frame of the Galaxy.

1. Logarithmic potential

The DF for the logarithmic potential of Eq. (33) can be written as

$$F(\epsilon, L_z^2) = (A+B)\exp\left(\frac{-2v^2}{v_0^2}\right) + C\exp\left(\frac{-v^2}{v_0^2}\right), \quad (A1)$$

where

$$A = F_0 4\pi \left(\frac{2}{\pi}\right)^{5/2} \left(\frac{v_\phi}{v_0}\right)^2 \frac{R_0^4}{(R_0^2+R_c^2)^2} \frac{1-q^2}{q^2}, \quad (A2)$$

$$B = F_0 4\pi \left(\frac{2}{\pi^5}\right)^{1/2} \frac{R_0^2 R_c^2}{(R_0^2+R_c^2)^2} \frac{1}{q^2}, \quad (A3)$$

$$C = F_0 \pi^{-3/2} \frac{R_0^2}{R_0^2+R_c^2} \frac{2q^2-1}{q^2}, \quad (A4)$$

and $F_0 = 0.47$ GeV cm$^{-3}/v_0^3$.

2. Power-law potential

The DF for the power-law potential of Eq. (37) for $\beta > 0$ can be written as

$$F(\epsilon, L_z^2) = A\,\widetilde{\epsilon}^{4/\beta-3/2} + B\,\widetilde{\epsilon}^{4/\beta-1/2} + C\,\widetilde{\epsilon}^{2/\beta-1/2}, \quad (A5)$$

where

$$\widetilde{\epsilon} \equiv \frac{\epsilon}{\Psi_a} = \frac{\Psi - \frac{1}{2}v^2}{\Psi_a} = \zeta^\beta - \frac{1}{2}\left(\frac{v}{v_1}\right)^2, \quad (A6)$$

with $\zeta = R_c/\sqrt{R_c^2+R_0^2}$, while the velocity $v_1 = \sqrt{|\Psi_a|}$ is fixed through Eq. (38), and with suitable normalizations, can be cast in the form

$$v_1 = 220 \text{ km sec}^{-1} \left(\frac{\rho_0}{0.47 \text{ GeV cm}^{-3}}\right)^{1/2} \frac{R_0}{8.5 \text{ kpc}}$$
$$\times \frac{q(R_c^2+R_0^2)^{(\beta+4)/4}}{\sqrt{|\beta|}R_0 R_c^{\beta/2}\sqrt{R_c^2(1+2q^2)+R_0^2(1-\beta q^2)}}. \quad (A7)$$

The quantities A, B and C may be written as

$$A = F_1 \left(\frac{v_\phi}{220 \text{ km sec}^{-1}}\right)^2 \left(\frac{R_0}{R_c}\right)^4$$
$$\times \frac{\Gamma(2+4/\beta)}{2^{3/2}\pi^{3/2}\Gamma(4/\beta-1/2)}\beta(\beta+2)\left(\frac{1}{q^2}-1\right), \quad (A8)$$

$$B = F_1 \left(\frac{v_1}{220 \text{ km sec}^{-1}}\right)^2 \left(\frac{R_0}{R_c}\right)^2$$
$$\times \frac{\Gamma(2+4/\beta)}{2^{3/2}\pi^{3/2}\Gamma(1/2+4/\beta)}\beta(\beta+2)\frac{1}{q^2}, \quad (A9)$$

$$C = F_1 \left(\frac{v_1}{220 \text{ km sec}^{-1}}\right)^2 \left(\frac{R_0}{R_c}\right)^2$$
$$\times \frac{\Gamma(2+2/\beta)}{2^{3/2}\pi^{3/2}\Gamma(1/2+2/\beta)}\beta\left[2-\frac{1+\beta}{q^2}\right], \quad (A10)$$

with $F_1 = 0.47$ GeV cm$^{-3}/v_1^3$.

For $\beta < 0$ Eq. (A5) still applies, with the following modifications (now $\Psi_a < 0$):

$$\widetilde{\epsilon} \equiv \frac{-\epsilon}{\Psi_a} = -\frac{\Psi + \frac{1}{2}v^2}{\Psi_a} = \zeta^\beta - \frac{1}{2}\left(\frac{v}{v_1}\right)^2, \qquad \text{(A11)}$$

where

$$A = F_1\left(\frac{v_\phi}{220 \;\; \text{km sec}^{-1}}\right)^2\left(\frac{R_0}{R_c}\right)^4$$

$$\times \frac{\Gamma(3/2 - 4/\beta)}{2^{3/2}\pi^{3/2}\Gamma(-1 - 4/\beta)}\beta(\beta + 2)\left(1 - \frac{1}{q^2}\right),$$

$$\text{(A12)}$$

$$B = F_1\left(\frac{v_1}{220 \;\; \text{km sec}^{-1}}\right)^2\left(\frac{R_0}{R_c}\right)^2$$

$$\times \frac{\Gamma(1/2 - 4/\beta)}{2^{3/2}\pi^{3/2}\Gamma(-1 - 4/\beta)}\beta(\beta + 2)\frac{1}{q^2}, \qquad \text{(A13)}$$

$$C = F_1\left(\frac{v_1}{220 \;\; \text{km sec}^{-1}}\right)^2\left(\frac{R_0}{R_c}\right)^2$$

$$\times \frac{\Gamma(1/2 - 2/\beta)}{2^{3/2}\pi^{3/2}\Gamma(-1 - 2/\beta)}\beta\left[\frac{1 + \beta}{q^2} - 2\right], \qquad \text{(A14)}$$

with again $F_1 = 0.47 \;\; \text{GeV cm}^{-3}/v_1^3$.

---

[1] For a recent review, see A. Morales, in *Proceedings of the VII Workshop on Topics in Astroparticle and Underground Physics* (TAUP2001), 2001, Italy, edited by A. Bellini, A. Bottino, and A. Dicredico [Nucl. Phys. B (Proc. Suppl.) **110**, 39 (2002)], astro-ph/0112550.

[2] DAMA/NaI Collaboration, R. Bernabei *et al.*, Phys. Lett. B **424**, 195 (1998); **450**, 448 (1999); **480**, 23 (2000).

[3] DAMA/NaI Collaboration, R. Bernabei *et al.*, Eur. Phys. J. C **18**, 283 (2000).

[4] P. Belli, R. Bernabei, A. Bottino, F. Donato, N. Fornengo, D. Prosperi, and S. Scopel, Phys. Rev. D **61**, 023512 (2000).

[5] A.K. Drukier, K. Freese, and D.N. Spergel, Phys. Rev. D **33**, 3495 (1986); K. Freese, J.A. Frieman, and A. Gould, *ibid.* **37**, 3388 (1988).

[6] DAMA/NaI Collaboration, R. Bernabei *et al.*, Phys. Lett. B **509**, 197 (2001).

[7] DAMA/NaI Collaboration, R. Bernabei *et al.*, Eur. Phys. J. C **23**, 61 (2001).

[8] A. Bottino, F. Donato, N. Fornengo, and S. Scopel, Phys. Lett. B **423**, 109 (1998); Phys. Rev. D **59**, 095003 (1999); **59**, 095004 (1999); **62**, 056006 (2000); **63**, 125003 (2001).

[9] R. Arnowitt and P. Nath, Phys. Rev. D **60**, 044002 (1999); E. Accomando, R. Arnowitt, B. Dutta, and Y. Santoso, Nucl. Phys. **B585**, 124 (2000); R. Arnowitt, B. Dutta, and Y. Santoso, hep-ph/0008336; J.L. Feng, K. Matchev, and F. Wilczek, Phys. Lett. B **482**, 388 (2000); E. Gabrielli, S. Khalil, C. Muñoz, and E. Torrente-Lujan, Phys. Rev. D **63**, 025008 (2001); D.G. Cerdeño, S. Khalil, and C. Muñoz, hep-ph/0105180; D.G. Cerdeño, E. Gabrielli, S. Khalil, C. Muñoz, and E. Torrente-Lujan, Nucl. Phys. **B603**, 231 (2001); M.E. Gómez and J.D. Vergados, Phys. Lett. B **512**, 252 (2001).

[10] N. Fornengo, in *Proceedings of the International Workshop on "Particle Physics and the Early Universe" (COSMO-98)*, Asilomar, Monterey, California, 1998, edited by D.O. Caldwell, AIP Conf. Proc. No. 478 (AIP, New York, 1999), p. 343; A. Bottino, in Proc. of the VIII International Workshop on "Neutrino Telescopes," Venice, 1999, edited by M. Baldo Ceolin, p.

203; R. Bernabei, *ibid.* p. 239; M. Brhlik and L. Roszkowski, Phys. Lett. B **464**, 303 (1999); A.M. Green, Phys. Rev. D **63**, 043005 (2001).

[11] J. Binney and S. Tremaine, *Galactic Dynamics* (Princeton University Press, Princeton, NJ, 1987).

[12] D. Lynden-Bell, Mon. Not. R. Astron. Soc. **136**, 101 (1967).

[13] J.D. Vergados, Phys. Rev. Lett. **83**, 3597 (1998); Phys. Rev. D **62**, 023519 (2000); C.J. Copi, J. Heo, and L.M. Krauss, Phys. Lett. B **461**, 43 (1999); P. Ullio and M. Kamionkowski, J. High Energy Phys. **03**, 049 (2001); J.D. Vergados and D. Owen, astro-ph/0203293.

[14] W. Jaffe, Mon. Not. R. Astron. Soc. **202**, 995 (1983).

[15] N.W. Evans, Mon. Not. R. Astron. Soc. **260**, 191 (1993).

[16] N.W. Evans, Mon. Not. R. Astron. Soc. **267**, 333 (1994).

[17] N.W. Evans, C.M. Carollo, and P.T. de Zeeuw, Mon. Not. R. Astron. Soc. **318**, 1131 (2000).

[18] J.F. Navarro, C.S. Frenk, and S.D.M. White, Astrophys. J. **462**, 563 (1996).

[19] B. Moore *et al.*, Mon. Not. R. Astron. Soc. **310**, 1147 (1990).

[20] A.V. Kravtsov *et al.*, Astrophys. J. **502**, 48 (1998).

[21] R.H. Helm, Phys. Rev. **104**, 1466 (1956).

[22] W. Dehnen and J. Binney, Mon. Not. R. Astron. Soc. **294**, 429 (1998).

[23] L.P. Osipkov, Pis'ma Astron. Zh. **55**, 77 (1979); D. Merrit, Astrophys. J. **90**, 1027 (1985).

[24] D. Lynden-Bell, Mon. Not. R. Astron. Soc. **120**, 204 (1960).

[25] M. Kamionkowski and A. Kinkhabwala, Phys. Rev. D **57**, 3256 (1998).

[26] F. Donato, N. Fornengo, and S. Scopel, Astropart. Phys. **9**, 333 (1999).

[27] S. Warren, P.J. Quinn, J.K. Salmon, and W.H. Zurek, Astrophys. J. **399**, 405 (1992); S. Cole and C. Lacey, Mon. Not. R. Astron. Soc. **281**, 7126 (1996).

[28] E.I. Gates, G. Gyuk, and M.S. Turner, Phys. Rev. D **53**, 4138 (1996).

[29] C.S. Kochanek, Astrophys. J. **457**, 228 (1996).

[30] M. Feast and P. Whitelock, Mon. Not. R. Astron. Soc. **291**, 683 (1997).